PHYSICAL REVIEW A **107**, 023105 (2023)

Real-space inversion and super-resolution of ultrafast scattering

Adi Natan[*]
Stanford PULSE Institute, SLAC National Accelerator Laboratory, 2575 Sand Hill Road, Menlo Park, California 94025, USA

(Received 14 July 2021; revised 20 January 2023; accepted 25 January 2023; published 6 February 2023)

Ultrafast scattering using x-rays or electrons is an emerging method to obtain structure dynamics at the atomic lengthscales and timescales. However, directly resolving in real-space atomic motions is inherently limited by the finite detector range and the probe energy. As a result, the time-resolved signal interpretation is mostly done in reciprocal space and relies on modeling and simulations of specific structures and processes. Here, we introduce a model-free approach to directly resolve scattering signals in real space, surpassing the diffraction limit, using scattering kernels and signal priors that naturally arise from the measurement constraints. We demonstrate the approach on simulated and experimental data, recover multiple atomic motions at sub-angstrom resolutions, and discuss the recovery accuracy and resolution limits versus signal fidelity. The approach offers a robust path to obtain high-resolution real-space information of atomic-scale structure dynamics using current time-resolved x-ray or electron scattering sources.

DOI: 10.1103/PhysRevA.107.023105

I. INTRODUCTION

Probing the structure and dynamics of systems of increased complexity with atomic resolution, ranging from small molecules in the gas phase to solute-solvent systems and disordered materials, is at the forefront of experimental research. Ultrafast scattering (unlike diffraction) usually refers to the diffuse scattering from atomic-size charge densities or angstrom-range structural correlations, using x-rays or electron pulses whose durations are below a picosecond. X-ray free-electron lasers (XFELs) and relativistic or high-energy electrons are sources of such pulses and have become powerful tools to study ultrafast atomic and molecular dynamics in chemical and solid-state systems at the angstrom and femtosecond scales.

In typical experiments that employ ultrafast scattering, an ultrashort optical "pump" pulse is used to photoexcite the system under study, and the probing is done at some time delay via an ultrashort x-ray or electron pulse that scatters from the sample. The time-delayed signal is usually subtracted from the signal of the unexcited sample to allow tracing changes in signal positions and infer structural dynamics. For example, this method was recently applied to probe molecules in the gas phase following single- and multiphoton excitations and chemical reactions [1–9], as well as structural changes of molecules in solution environments [10–16].

Directly obtaining real-space time-resolved information by inversion of the scattering pattern is often not possible in these studies because of the limited available range of the scattering vector, severely restricting the spatial resolution. To address this issue, the methods that were developed to interpret the scattering signals were system-dependent, and they relied on calculating and attaining trajectory statistics. These methods were mostly restricted to the reciprocal q-space [2,17], and they were often limited to a particular reaction pathway. Complex atomic motions of general polyatomic systems that take place simultaneously and involve multiple pathways at sub-angstrom distances are theoretically challenging to model and were not directly resolved in experiments.

Here we demonstrate a robust and model-free deconvolution approach to overcome the limitations that are imposed by a typical inversion procedure, extending super-resolution methods that have recently transformed optical microscopy and biological imaging [18–22] to applications where only restricted scattering information is present, with no access to high spatial frequencies, multiple scattering, or single emitters. Our approach does not require a pool of calculated structures, or assume any structure at all, making it attractive for capturing general motions that may contain density distributions beyond atomic positions, such as wave-packet motion, as well as differential signals where an undetermined subset of the system contributes to the measured motion.

We show how real-space recovery of multiple and complex motions of general polyatomic systems can be obtained by leveraging the information and constraints that naturally arise from the measurement configuration and analysis procedure. We derive a formalism to express the way a set of scattering kernels, which are effectively position-dependent point spread functions in ultrafast scattering experiments, can be used to capture general distortions in the inversion procedure. We then use regularization and convex optimization to recover and super-resolve real-space atomic motions as a sparse or smooth solution of a dictionary of scattering kernels. While the approach is applicable for x-ray, electron, and neutron scattering, for brevity we will discuss mostly the case of x-ray scattering.

II. METHOD

To describe angstrom and femtosecond scale dynamics of general molecular systems, it is not valid to assume sample

---

[*] natan@stanford.edu

periodicity. As a result, the scattering patterns are often broad and diffuse, capturing short-range spatial correlations. Diffuse x-ray scattering of time-evolving charge densities is generally inelastic, but under typical experimental conditions the general electronic scattering operator can be replaced with its elastic expression [23,24]. In experiments, the signal is usually integrated over an angle for improved fidelity, and the isotropic signal was shown to contain all the nuclear and electronic structural evolution of the charge density [25]. For simplicity, we will introduce the approach using the isotropic scattering signal given by the Debye equation [26,27]:

$$S_0(q,\tau) = \sum_a f_a(q)^2 + \sum_a \sum_{b\neq a} f_a^*(q) f_b(q) \times 4\pi \int_0^\infty dR\, R^2 \rho_{ab}(R,\tau) j_0(qR), \tag{1}$$

where $S_0(q,\tau)$ is the isotropic diffuse scattering signal at time delay τ, $q = 4\pi \sin(\theta_q/2)/\lambda$ is the scattering vector magnitude, with the scattering angle θ_q and wavelength λ, the double sum is over all atom pairs, $f_i(q)$ is the atomic form factor of the ith atom, $\rho_{ab}(R,\tau)$ is the pair charge density, and $j_0(qR) = \sin(qR)/qR$ is the zeroth-order spherical Bessel function of the first kind.

For the case of ultrafast scattering, the scattering signal difference $\Delta S_0(q,\tau) = S_0(q,\tau) - S_0(q,0)$ is often analyzed, and as a result, the stationary atomic form-factor term $\sum_a f_a(q)^2$ in Eq. (1) cancels. Without loss of generality, we will therefore consider the scattering difference signal to demonstrate the approach to recover the isotropic real-space difference pair density $\Delta\rho_{ab}$. The Debye equation is related to the real-space pair correlation function through a Fourier transform [28]. For isotropic signals, direct real-space inversion of Eq. (1) can be done for the case of a single pair density contribution:

$$\Delta\rho_{ab}(R,\tau) = \int_0^\infty dq\, q^2 \frac{\Delta S_0(q,\tau) j_0(qR)}{f_a(q) f_b(q)}. \tag{2}$$

The integrand here is often scaled with an exponential function e^{-kq^2} [11,29] that serves as an effective experimental integration bound; however, this formalism does not capture various aspects of the measurement, such as the experimental configuration, sample thickness, detector truncation, and discretization. As a result, applying Eq. (2) to experimental ultrafast scattering signals will yield inversion artifacts in addition to the diffraction-limited resolution, especially around the few angstrom lengthscale that is relevant for structural dynamics of atomic and molecular systems.

To illustrate this, in Fig. 1 we show the inversion of a Dirac δ charge density of a single-atom pair at 3 Å. We assume typical experimental conditions for gas phase scattering similar to [3], e.g., 9 keV photon energy, a sample thickness of 8 mm, located 60 mm from a finite detector, a limited q-range $0.5 < q < 4$ Å^{-1}, resulting in a diffraction-limited spatial resolution given by $2\pi/q_{\max} \simeq 1.57$Å. The inverted waveform in Fig. 1(c) fails to accurately recover the original δ-function position as it is distorted by the scattering integrated over the sample thickness and q-range truncation. This example provides us with a path to define a natural scattering kernel (NSK), or the function that describes the distortion that a δ-function charge density naturally undergoes in terms of measurement in q-space and inversion analysis in real space. Because we can express any pair density as a weighted sum of δ functions in real space, we would like to explain the distorted inversion of experimental signals as a weighted sum of NSKs. We will describe the considerations to obtain these kernels, and the way they can be used to recover and super-resolve real-space motions.

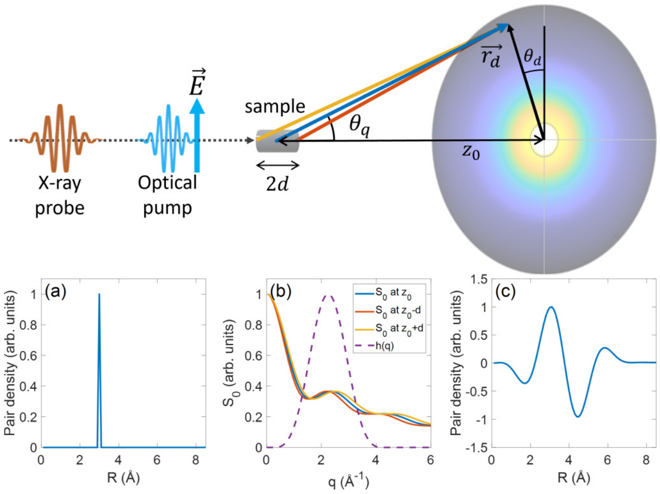

FIG. 1. Top: A sketch of a typical optical pump x-ray scattering probe experimental configuration, with sample thickness $2d$ located z_0 away from a finite detector. We illustrate how the scattering on the detector at a radius r_d is the sum of different parts of the sample (depicted as yellow, blue, and red lines) as explained below. (a) A Dirac δ at 3 Å is used as the initial pair density. We model the scattering assuming sample thickness and distance from a detector similar to that in Ref. [3]. (b) The isotropic scattering curves $S_0(q)$ from the sample center at z_0 (blue) vs the sample edges at $z_0 \pm d$ (red and yellow) added to the same spot in the detector, creating a signal distortion. The scattering is also truncated due to the finite detector dimensions and q-dependent absorption, modeled by the window function $h(q)$. (c) The inversion of scattering, including measurement constraints, describes how the distortion propagates to real space, where the retrieved pair density fails to accurately describe the initial density.

A. Distortions in q-space

The experimental configuration and finite detector may introduce signal distortions to the measured scattering pattern, as seen in Fig. 1. We can express the relation between the scattering vector magnitude q, the distance of the sample from the detector z, and the radial position on the detector $r_d = \sqrt{x^2 + y^2}$ by

$$q(z) = \frac{4\pi}{\sqrt{2}\lambda} \sqrt{1 - \frac{z}{\sqrt{r_d^2 + z^2}}}, \tag{3}$$

where the origin of the coordinates is located at the center of the detector, and we assume that the dimensions of the optical-x-ray pump-probe interaction area are much smaller than the sample thickness (typically microns versus millimeters). A general distortion of the scattering signal in q-space can be expressed by

$$\tilde{S}_0(q,\tau) = \int_{z_0-d}^{z_0+d} dz\, h(q(z))\, S_0(q(z),\tau) + b(q(z)), \qquad (4)$$

where $\tilde{S}_0(q,\tau)$ is the scattering signal measured on the detector, which is distorted by the measurement constraints, S_0 was defined in Eq. (1), and we assume a sample thickness of $2d$ at a distance of z_0 from the detector. We define $q = q(z_0)$ at the sample center, $b(q)$ is a possible additive background, and $h(q)$ is a window function that represents the detector's finite q-range as well as q-dependent signal absorption. In experiments, the shape of $h(q)$ may also be affected by the sample density profile, propagation-related absorption, and detector-dependent attenuation related to the experimental setup design. These can be accounted for in calibration measurements, for example in [30].

In this context, it is assumed that the measured signal has been adjusted for factors such as x-ray polarization, detector geometry, and nonlinear response, as described in [31]. In the analysis stage, a smooth modification function, such as the Slepian or Lorch function [32], is often applied to reduce the signal cutoff at the edges of the detected q-range. The function $h(q)$ takes into account these modification functions, as well as any other relevant contributions mentioned.

B. Discretization

Because the measured scattering signal is discretized by the detector at some resolution, but the inversion in Eq. (2) is a continuous transform, we would like to use a resampling and discretization scheme that maintains the transform's orthogonality and operational rules, such as discrete shift, multiplication, and convolution, between the R and q domains. Using the Bessel-Fourier expansion [33] and the standard Shannon sampling theorem [34], we define

$$\{q_i\}_1^N = \frac{j_{0i}}{j_{0N}} N\Delta q, \quad \{R_m\}_1^M = \frac{j_{0m}}{M\Delta q}, \qquad (5)$$

where we assume detector discretization Δq, with an experimental upper bound $q_{\max} = N\Delta q$, and we resample the scattering signal at q_i, given by j_{0i}, the ith root of the spherical Bessel function j_0. The ratio M/N is an effective super-resolution factor [35] that can be used to determine the final recovery resolution of noisy signals for a given signal-to-noise ratio (SNR).

C. Inversion

The distorted difference scattering signal is discretized $\Delta\tilde{S}_0(q_i,\tau)$ and inverted using the resampling scheme we introduced in Eq. (5) by

$$\Delta \mathrm{PD}_0(R,\tau) = \frac{[(M-1)\Delta q]^2}{j_{0M}} \sum_{i=1}^{M-1} \boldsymbol{G}_{mi} \frac{\Delta\tilde{S}_0(q_i,\tau) q_i}{f_e(q_i)}, \qquad (6)$$

where $\Delta\mathrm{PD}_0$ is the discretized pair density difference, $f_e(q_i) = \sum_{b\neq a} f_a(q_i) f_b(q_i)$ is an effective form factor, and the transformation kernel is given by

$$[\boldsymbol{G}]_{mi} = 2\frac{j_0\left(\frac{j_{0m} j_{0i}}{j_{0M}}\right)}{j_{0M}\, j_1^2(j_{0i})}, \qquad (7)$$

where $j_1(j_{0i})$ is the first-order spherical Bessel function evaluated on the ith root of j_0. The derivation of $\boldsymbol{G}$ is obtained in a similar fashion to the derivation done for the discrete Hankel transform [33], adapted here for the case of spherical Bessel functions. We note that f_e is an approximation needed in cases in which the scattering signal is composed of several atom pair types with different form factors that are not separable in the analysis process, as only the total signal $S_0(q,\tau)$ is measured. The approximation is justified because each $f_a(q) f_b(q)$ term is a featureless monotonic function in the truncated q-range, and so its real-space inversion will mainly contribute to the amplitude at $0 < R < \pi/q_{\max}$. As a result, any inaccuracy using f_e will be limited to an amplitude artifact in that range, because it is in the sub-angstrom range, which is smaller than typical bond lengths for typical ultrafast scattering experiments.

To invert the total scattering signal $S_0(q_i,\tau)$, we can replace $\Delta\tilde{S}_0(q_i,\tau)$ in Eq. (6) with $\tilde{S}_0(q_i,\tau) - \sum f_a(q_i)^2$.

To clarify the steps above, we will consider the following example: We solved a time-dependent Schrödinger equation (TDSE) for diatomic iodine with parameters similar to [3], 30 fs pulses at 520 nm, with an 8% excitation fraction. At a delay of $\tau = 150$ fs, the calculated density difference $\Delta\rho(R,\tau)$ features a depleted ground state at 2.67 Å, with bound and dissociative excited states at 3.9 and 4.7 Å [Fig. 2(a)]. We simulated the scattering signal difference from this delay assuming the experimental conditions mentioned earlier (8 mm sample width, 60 mm from a detector), with $\Delta q = 0.1$ Å^{-1}, and a q-range of $0.5 < q < 4$ Å^{-1} that is modeled as $h(q)$ by a Slepian window function ($N = 40$ sampling points in q). The choice of Δq magnitude was to capture details in real space limited by $R_{\max} = \pi/\Delta q \simeq 31.4$ Å.

We applied the inversion step using real-space discretization at a resolution of $\Delta R \simeq 0.157$ Å (1/10 the diffraction limit for the q-range considered). The value of ΔR is attained by choosing $M = \mathrm{ceil}(\pi/(\Delta R \Delta q)) + 1$ sampling points, resulting with a super-resolution factor $M/N \simeq 5$. The inverted pair density difference $\Delta\mathrm{PD}_0(R,\tau)$ in Fig. 2(a) cannot resolve the two excited states, as their separation ∼0.8 Å is below the diffraction limit (∼1.57 Å). Additionally, the measurement constraints cause $\Delta\mathrm{PD}_0(R,\tau)$ to be distorted, creating a structure that bears little resemblance to the initial charge density, as demonstrated by the positive peak at 1 Å and the negative peak around 5.5 Å.

D. Dictionary formation

We will implement the steps above: the q-space distortion, discretization, and inversion, for a Dirac δ pair density, by substituting $\rho_{ab}(R) = \delta(R - R_m)$ in Eq. (1), as seen in Fig. 1(c) for the case $R_m = 3$ Å. The result will be the real-space distorted inversion of the δ function for position R_m, expressed by

$$\mathrm{NSK}(R_m) = \frac{[(M-1)\Delta q]^2}{j_{0M}} \sum_{i=1}^{M-1} \boldsymbol{G}_{mi}\, \tilde{j}_0(q_i R_m) q_i, \qquad (8)$$

where

$$\tilde{j}_0(qR_m) = \int_{z_0-d}^{z_0+d} dz\, h(q(z))\, j_0(q(z)R_m). \qquad (9)$$

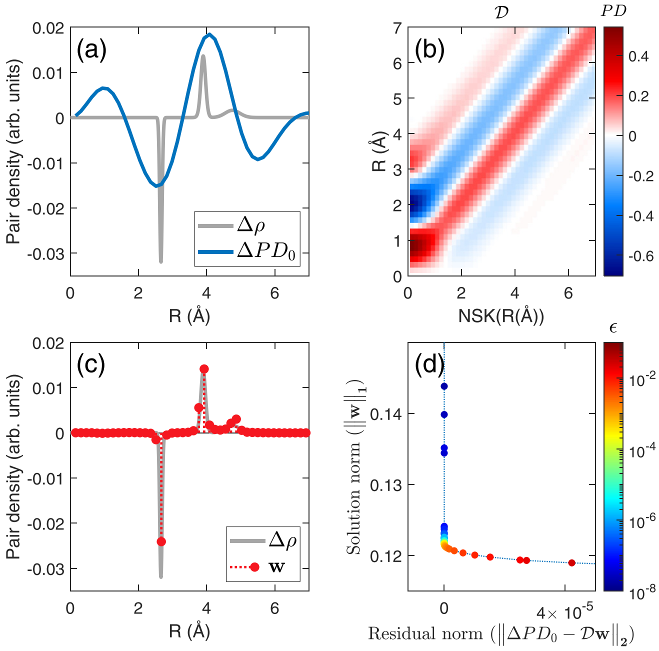

FIG. 2. (a) The simulated pair density difference $\Delta\rho(R,\tau)$ of excited diatomic iodine at a pump-probe delay of $\tau = 150$ fs is used to obtain the inverted pair density difference $\Delta\mathrm{PD}_0$ [Eq. (6)], distorted by the truncated q range $0.5 < q < 4$ Å^{-1}, and the experimental conditions in [3]. (b) Using the measurement constraints, we form the NSK dictionary $\mathcal{D}$ and apply convex optimization for the ℓ_1 regularization case [Eq. (11)]. (c) We obtain the weights vector $\mathbf{w}$ solution (red stem) that is in excellent agreement with the theoretical pair density, resolving peak positions and amplitudes separated by 0.8 Å, below the diffraction limit ($\simeq$1.57 Å). (d) To obtain the optimal value of the regularization parameter ϵ in Eq. (11), we use the L-curve method, plotting the solution norm vs the residual norm for a logarithmic range in ϵ, and using the value of ϵ found at the corner of the L-shaped region (see the text).

For very thin samples where we can take $d \to 0$ such as in the case of micron width liquid jets, we can approximate $\tilde{j}_0(qR_m) \simeq j_0(qR_m)h(q)$.

The NSKs are system-agnostic as the effective form factor f_e that was used for the inversion of a general measured signal cancels for the case of the kernels, and the expression in Eq. (8) simplifies to contain only the distorted $\tilde{j}_0(qR_m)$. We can now create a set of NSKs along the real-space sampling given by Eq. (5) to assemble a dictionary of the following form:

$$\boldsymbol{\mathcal{D}} = \begin{bmatrix} | & & | & & | \\ \mathrm{NSK}(R_1) & \cdots & \mathrm{NSK}(Rm) & \cdots & \mathrm{NSK}(R_M) \\ | & & | & & | \end{bmatrix}.$$

In Fig. 2(b) we describe an NSK dictionary assuming the experimental conditions used in the example, similar to [3]. The observed position-dependent point spread function shape of the kernels is dominated by the shape of $h(q)$, which serves as a band-pass filter in q-space.

E. Deconvolution

We would like to use the NSKs dictionary we derived to explain the inversion signal that is distorted by the measurement constraints, assuming the linear model:

$$\Delta\mathrm{PD}_0 = \boldsymbol{\mathcal{D}}\mathbf{w}, \tag{10}$$

where we seek to estimate the weights vector $\mathbf{w}$ to recover the pair density described by $\Delta\rho(R) = \sum_m \mathrm{w}_m \delta(R - R_m)$.

Naively, one would attempt to solve this model using least-squares minimization: $\min_{\mathrm{w}} \|\Delta\mathrm{PD}_0 - \boldsymbol{\mathcal{D}}\mathbf{w}\|^2$, however this approach is highly sensitive to noise and is generally unstable numerically when the problem is ill-posed. A standard approach for solving ill-posed inverse problems is to use a regularization framework of the form

$$\min_{\mathrm{w}} \|\Delta\mathrm{PD}_0 - \boldsymbol{\mathcal{D}}\mathbf{w}\|^2 + \epsilon\mathcal{R}(w), \tag{11}$$

where the regularizer $\mathcal{R}(\mathbf{w})$ is chosen according to some prior information of the measurement to promote solutions with preferable features such as sparsity or smoothness, and ϵ controls the magnitude of the regularization and can be estimated via the L-curve method or by cross-validation [36,37]. For the examples discussed here, we will implement the L-curve method.

Briefly, this curve is obtained when plotting the penalty term of the regularized solution norm $\mathcal{R}(\mathbf{w})$ versus the residual norm $\|\Delta\mathrm{PD}_0 - \boldsymbol{\mathcal{D}}\mathbf{w}\|_2^2$ for a logarithmic range of ϵ values, creating a characteristic L-shape, where $\|\cdot\|_2$ is the Euclidean norm. The ϵ value that corresponds to the corner of the L-curve, where the curvature is maximal, captures the best tradeoff between minimizing the residual norm and the penalty term that captures the nature of the solution. An implementation of the L-curve method is shown in Fig. 2(d) for the example we discuss.

For the regularizer $\mathcal{R}(\mathbf{w})$, we will discuss two approaches, promoting smooth or sparse solutions. A widely used approach that addresses the numerical instabilities and produces low variance solutions is the Tikhonov or ℓ_2 regularization [38], for which $\mathcal{R}(\mathbf{w}) = \sum_m |\mathrm{w}_m|^2$. Using this regularizer provides the closed-form linear solution $\mathbf{w} = (\boldsymbol{\mathcal{D}}^T\boldsymbol{\mathcal{D}} + \epsilon\mathbf{1})^{-1}\boldsymbol{\mathcal{D}}^T\Delta\mathrm{PD}_0$ that can be solved using singular value decomposition. This approach promotes stable and smooth solutions and increases the ability to predict their nature. However, it also often results in most of the $\mathbf{w}$ elements having nonzero values, which may reduce the ability to resolve or explain weaker signals.

For the case in which we assume that the solution for $\mathbf{w}$ is sparse, such that the number of sampling points in R that can explain the distorted $\Delta\mathrm{PD}_0$ is much smaller than M, we can use the ℓ_1 regularized least-squares model [39,40], where $\mathcal{R}(\mathbf{w}) = \sum_m |\mathrm{w}_m|$. While this case does not have a closed-form solution, it can be solved using convex optimization, and can lead to super-resolution. In recent years, several algorithmic approaches have evolved to solve this model, determine the optimal parameters [41–43], and provide applications that transformed areas of research such as statistics, machine learning, and signal processing [35,44–54].

In Fig. 2(c) we applied convex optimization for the ℓ_1 regularization case [Eq. (11)] for the pair density difference and the NSK dictionary shown in Figs. 2(a) and 2(b) using CVX, a package for specifying and solving convex programs [55].

We find the optimal regularization parameter ϵ using the L-curve method [Fig. 2(d)]. We note that the solution obtained is robust for a wide range of ϵ values around the corner of the L-curve. The solution given by the weights vector $\mathbf{w}$ is in excellent agreement with the theoretical pair density difference, super-resolving the excited states pair-density positions and amplitudes while eliminating the distortions in $\Delta\mathrm{PD}_0$.

We note that the case presented here differs from some of the approaches referenced above that also used ℓ_1 regularized least-squares. This is because the NSK dictionary is highly correlated, each kernel is similar to its adjacent neighbors, and so the restricted isometry property that is needed in compressed sensing schemes [35] is not satisfied here. As a result, an additional restriction is introduced in the form of a minimum separation distance between adjacent NSKs to avoid solution ambiguity below some $\delta R < \nu/q_{\max}$ that depends on the signal's properties and fidelity [56–58]. In the next section, we will discuss the conditions for super-resolution and find the minimum separation distance for noisy signals.

III. RECOVERY ACCURACY FOR NOISY SIGNALS AND SUPER-RESOLUTION

Super-resolution in the context of scattering means to resolve at least two pair distances below the diffraction limit given by $2\pi/q_{\max}$. The accuracy of the recovery method presented and the ability to achieve super-resolution depend both on the SNR and the super-resolution factor. To robustly super-resolve using NSKs and ℓ_1 regularization, an additional minimum separation distance is introduced [56]. To obtain its value and characterize the recovery accuracy, we consider the case when two pair distances approach each other, and we focus on the recovery accuracy as a function of SNR.

We use a three-atom model system, similar to CO_2 (Fig. 3), where we fix the positions of the outer atoms (A, C) to $x = \pm 2$ Å while changing the position of (B) the central atom $(-1 < x < 1$ Å). When atom B is at $x = 0$, the pair distance R_{AB} will merge with R_{BC} at 2 Å. We applied the same experimental configuration used in [3] and in the previous example, q-range $0.5 < q < 4$ Å^{-1} with the discretization $\Delta q = 0.1$ Å^{-1}, and we simulated the scattering signal for each of the distances. To test the recovery accuracy, we added to the total scattering signal q-dependent additive white Gaussian noise, where each q_i bin has sampling statistics proportional to the number of detector pixels contributing to it, assuming the array detector in [31].

We applied the NSK approach with sampling $\Delta R \simeq 0.05$ Å, and we tested the recovery for a range of single detector pixel SNRs (−15 to 30 dB), with 20 realizations to each noise level to obtain recovery statistics. We find that the recovery accuracy for the ℓ_1 regularization is proportional to the noise level, demonstrating the stability of the approach, and in agreement with theory [56]. For the fixed R_{AC} distance, the recovery error is <0.1 Å across the SNRs [Fig. 3(d)], demonstrating the accuracy of the approach for the case of well-separated pair distances [Fig. 3(c)]. For the case in which the two pair distances R_{AB} and R_{BC} approach each other, we obtain a separation of $\delta R \simeq 0.35 \pm 0.15$ Å that allows robust recovery below the diffraction limit (≃1.57 Å) for the SNR range used [Fig. 3(e)]. The minimal separation distance is derived from the recovery error statistics, where we observe that the recovery error is due to both noise and a coalescence effect where both distances drift toward the joint center of mass [Fig. 3(f)]. The coalescence effect is unique to the super-resolution case. It has quadratic dependence in the super-resolution factor M/N [56], and it takes place when two adjacent NSKs explain effectively the same noisy distorted measurement. As a result, the ℓ_1 regularization that acts as a sparsity prior to the recovery will instead promote a single NSK solution at the midpoint to explain the same measurement.

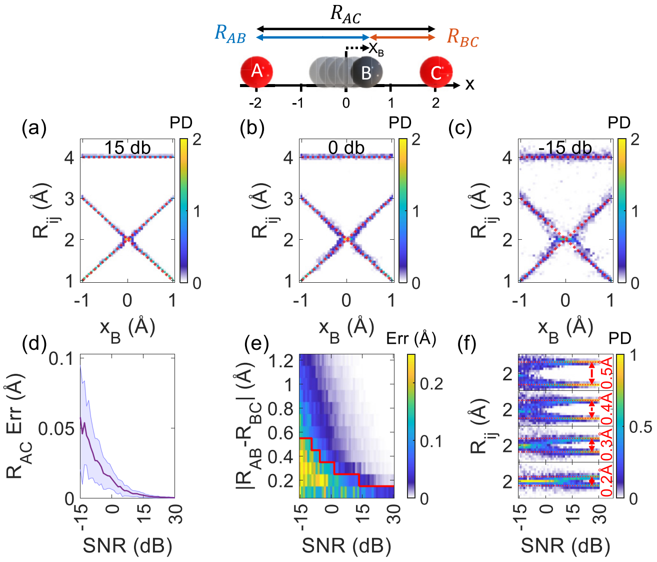

FIG. 3. Recovery accuracy under noise is tested for a three-atom system (top), where two pair-distances (R_{AB}, R_{BC}) approach each other below the diffraction limit. The scattering is simulated for each atom B position, truncated by $0.5 < q < 4$ Å^{-1}, and inverted using NSKs (ℓ_1 regularization). The diffraction limit for this case is $2\pi/q_{\max} \simeq 1.57$. The inversions for (a) 15, (b) 0, and (c) −15 dB SNRs are shown vs exact distances (dotted red), and PD is normalized by the total charge density. The recovery error is proportional to the SNR, validating the stability of the approach. (d) For R_{AC} distance, the average recovery error (solid) and standard deviation (shaded) are <0.1 Å across SNRs. The conditions for super-resolution and minimal separation emerge when the R_{AB}, R_{BC} distances approach each other. (e) The average recovery error (Err) is plotted as a function of pair separation $|R_{AB} - R_{BC}|$ and SNR, and used to define the minimal separation at which both distances are resolved (solid red). (f) The recovery in the super-resolution regime for different separations compared with the exact distances (dotted red) is limited by both SNR and the pair coalescence effect (see the text). We obtain that the diffraction limit is surpassed by a factor 3.1–7.8 for the range of −15 to 30 db.

The minimum separation is defined as the distance where the average recovery error due to the coalescence effect is equal to half the distance between each pair and their joint center of mass, at a given SNR and M/N. Inaccuracy in the recovery due to this limitation can be addressed by adjusting M/N given by the real-space resampling, to be compatible with the estimated measured SNR. The minimal separation distance acts as the *de facto* resolution limit for an unknown sparse charge density distribution for the case of super-resolution in noisy conditions. Applying to the recovered density an additional real-space blur of the same width can be done to ensure the objectivity of the result for cases in which the sparse density might contain features below the minimum separation. The implementation of the NSK approach for general anisotropic signals of arbitrary order can be found in the Appendix.

IV. RESULTS

A. Numerical demonstration: Wave-packet dynamics in iodine

We revisit the numerical example shown in Fig. 2 and consider a broader range of time delays, $0 < \tau < 1.8$ ps, capturing the evolving coherent nuclear wave-packet dynamics that undergo multiple motions such as dissociation and anharmonic vibrations. We simulated the scattering signal with the same measurement constraints of the previous example ($0.5 < q < 4$ Å^{-1}), and we assumed an SNR of 20 dB per detector pixel on the scattering difference signal $\Delta\tilde{S}_0(q,\tau)$. We inverted the truncated signal to obtain $\Delta\text{PD}_0(R,\tau)$ and used the dictionary of NSKs with the same measurement constraints to deconvolve the distorted $\Delta\text{PD}_0(R,\tau)$ using the ℓ_2 regularization, as seen in Fig. 4(c). While this approach handles some of the inversion artifacts, the nature of the smooth solutions it promotes reduces the ability to resolve weaker signals and does not achieve super-resolution.

In Fig. 4(d), we applied convex optimization for the ℓ_1 regularization case [Eq. (11)], the minimal separation found in the previous section, and we managed to accurately capture real-space information and to super-resolve details below 0.4 Å. For example, we were able to resolve the wave-packet positions and dispersion surpassing the diffraction-limited recovery that was obtained for the case of ℓ_2 regularization.

B. Experimental demonstration: Ring-opening dynamics in CHD

In Fig. 5, we applied the NSK inversion approach using the ℓ_1 regularization to data collected by an ultrafast electron scattering experiment that captured the photoinduced ring-opening of 1,3-cyclohexadiene (CHD) [7]. This well-studied polyatomic molecule has 14 atoms and a total of 91 atom pairs in three groups (C-C, C-H, H-H). We used the effective form-factor approximation to invert the experimental signal at 0.55 ps delay, as the structural opening of the ring takes place and 1,3,5-hexatriene (HT) isomers are formed. We analyzed the scattering signal with the same binning as in the inversion of [7], $\Delta q = 0.0974$ Å^{-1}, q-range truncation $1.3 < q < 10.2$ Å^{-1}, and we used an NSK spatial resolution of $\Delta R \simeq 0.1$ Å, which corresponds to a super-resolution factor $M/N \simeq 3.1$. We estimated -16 db SNR per pixel of the measured difference data by comparing it with simulated scattering signals derived from the *ab initio* multiple spawning (AIMS) simulations, done at the α-CASSCF(6,4)/6-31G* level of theory [7].

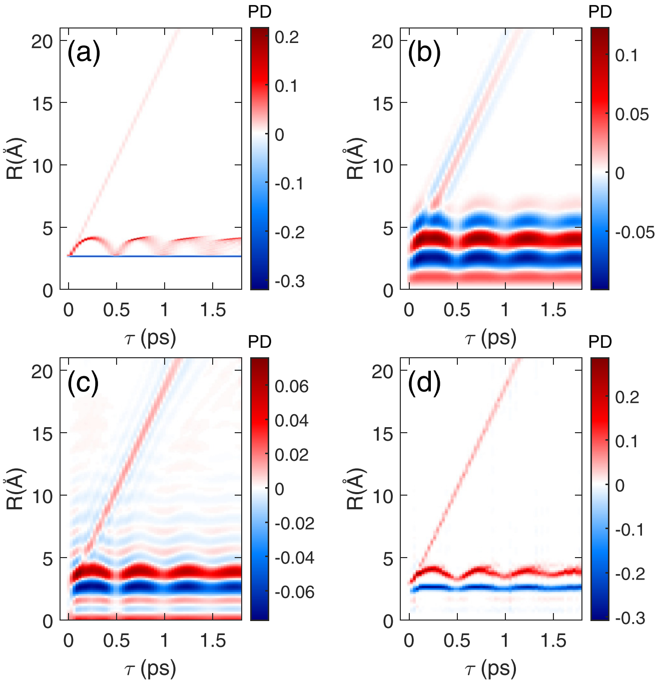

FIG. 4. (a) TDSE calculation of the time-dependent charge density difference (PD normalized to the total charge) for diatomic iodine resulting in coherent vibration and dissociation wave-packet motions. Simulating its difference scattering signal assuming typical experimental conditions similar to [3] and adding noise (20 db SNR), we (c) inverted the truncated signal difference and obtained the pair-density difference signal. The limited q-range hinders the ability to recover the positions and motions of the calculated charge density. The NSK dictionary formed by the measurement constraints was used to deconvolve the distorted pair density using (c) ℓ_2 and (d) ℓ_1 regularization. For the ℓ_1 case, we obtain super-resolution in the recovery, resolving multiple motions and wave-packet shape dispersion.

We inferred a minimum separation distance of $\delta R \simeq 0.15$ Å by performing a noise analysis procedure similar to the one discussed in the previous section using the q-range reported in the experiment. The minimal separation distance was then used to blur the ℓ_1 regularization solution seen in Fig. 5(a).

We are able to resolve <0.3 Å features, including details of several individual pair distances that were not resolved by the inversion done in [7]. Our results are in excellent agreement with the AIMS trajectories without further processing the trajectories in the same way as the experimental inversion done in [7]. We observe the depletion of the initial steady-state C-C distances at 1.4, 2.5, and 2.85 Å, and C-H distance at 1.05 and 2.1 Å as new distances >3 Å form due to the ring opening. The new distances correspond to C-C and C-H pairs of the HT isomers. We find that the C-H pair distances significantly contribute and are better markers for the structural dynamics of the ring opening process due to the relative rigidity of the C-H bond. The details of the inversion we perform facilitate a quantitative understanding of the different contributions of the different HT isomers and help elucidate structure beyond 3 Å that cannot be attributed to a combination of the isomer structures.

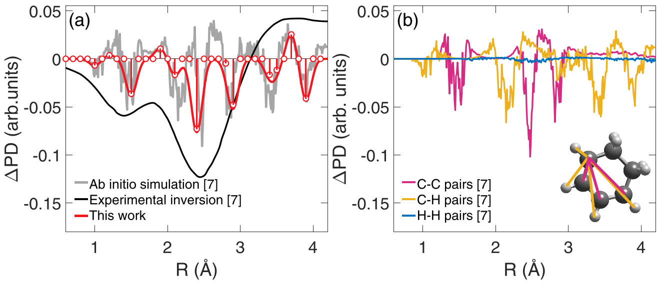

FIG. 5. (a) *Ab initio* multiple spawning trajectories simulation (gray) and experimental pair density difference (black) of photoinduced ring-opening of CHD at 0.55 ps from [7] vs the inversion and super-resolution of the experimental data using the NSKs method presented here (red). The NSKs solution uses ℓ_1 regularization (red circles), following the minimal separation assumption given the estimated measurement noise (solid red). Individual peaks, resolved at <0.3 Å resolution, correspond to atom pair distances that significantly change during the ring-opening: positive peaks point to new distances that are formed as the ring opens, while negative peaks point to depletion of steady-state distances. The details resolved surpass the diffraction limit ($\simeq$0.62 Å) for the measurement by a factor of >2. (b) The pair composition of the simulated charge density difference highlights the depletion of the C-C (pink) and C-H (yellow) distances that are resolved by the NSK method. These distances are illustrated in the CHD steady-state geometry (inset).

V. CONCLUSION

In summary, we have developed a model-free approach to directly resolve scattering signals in real space, beyond the diffraction limit. We validate the approach using simulated and experimental scattering data. We demonstrate super-resolution of simultaneous motions *de novo* and discuss the resolution limits as a function of fidelity.

This approach opens the way to directly trace the spatiotemporal shape of coherent wave-packet motions and energy redistribution of different atom-pairs that take place simultaneously, without bias toward the Franck-Condon active modes or the constraints of normal mode analysis. This approach can be further extended considering different regularization schemes such as the elastic net [59], off-the-grid type methods [60], and the addition of temporal dependence of the regularizer to further constrain the dynamics. The approach also allows the inclusion of other aspects of the scattering process, such as resonant scattering, inelastic and coherent scattering cross-terms, or self-scattering as in the case of laser-induced electron diffraction [24,61–67].

The approach is especially beneficial for high-fidelity scattering signals that are expected from high-repetition rate instruments that are becoming available, and it may help to bridge the established pair-distribution function analysis that requires much higher q ranges (>30 Å^{-1}) with time-resolved high-energy (15–25 keV) x-ray scattering and electron scattering experiments, which have just begun recording high-fidelity transient signals in the $q \sim 10$ Å^{-1} range.

ACKNOWLEDGMENTS

We thank T. J. A. Wolf, D. M. Sanchez, and T. J. Martínez for the experimental data and *ab initio* trajectory simulations in [7]. This work was supported by the U.S. Department of Energy, Office of Science, Basic Energy Sciences, Chemical Sciences, Geosciences, and Biosciences Division.

APPENDIX: SCATTERING AND INVERSION FOR ANISOTROPIC CHARGE DENSITIES

In ultrafast scattering studies, the dynamics of a photoexcited ensemble of molecules are usually captured in a pump-probe scheme, where the excitation pump pulse is usually a linearly polarized ultrafast optical pulse with a duration shorter than the typical timescales of motion of interest. Integrating the angle information of the scattering signal is well justified as it captures all types of motions that take place in the photoexcited system; however, often there is an inherent anisotropy in the scattering signal when a sample is excited by linearly polarized light due to an optically induced dipole moment transition. The photoabsorption process creates charge density anisotropy in the ensemble, which can be used to filter and enhance the specific processes under study, such as in the case of a single-photon absorption process [3,15,68], as well as excitation of a higher number of photons [5,69].

We will consider the real-space general anisotropy information of photoexcited molecular systems and derive the corresponding anisotropic scattering curves $S_n(q, \tau)$ using results that have been derived elsewhere [5,23,25,68]. We assume that both the x-ray pulse and the optical laser pulse are copropagating along $\mathbf{k_0}$ and that the angle between the incident x-ray beam and the laser polarization is $\pi/2$, which allows us to employ a Legendre decomposition in angle space. The expression for the differential cross-section difference scattering is

$$\Delta\frac{d\sigma}{d\Omega} = \sigma_T \int d\mathbf{R}\Delta\rho(\mathbf{R}, \tau)|F(\mathbf{q}, \mathbf{R})|^2,$$

$$F(\mathbf{q}, \mathbf{R}) = \sum_{b\neq a} f_a^*(q) f_b(q) e^{\imath \mathbf{qR}}, \tag{A1}$$

where σ_T is the Thomson cross-section, $\Delta\rho$ is the charge density difference, and the squared molecular form factor $|F|^2$ is invariant under space inversion $R \mapsto -R$, with the scattering vector $\mathbf{q} = \mathbf{k_s} - \mathbf{k_0}$ and the (double) sum is over all atom pairs. We can expand the scattering exponential term using the plane-wave expansion:

$$e^{\imath \mathbf{qR}} = \sum_{n=0,2,\ldots} (2n+1)(-1)^{n/2} P_n(\cos\theta_{qR}) j_n(qR), \tag{A2}$$

where P_n are Legendre polynomials, j_n are spherical Bessel functions, and θ_{qR} is the angle between $\mathbf{q}$ and $\mathbf{R}$. We sum only over even orders as odd polynomial components are antisymmetric under space inversion and will cancel for the differential cross-section. Using the spherical harmonics addition theorem, we expand the Legendre polynomials to express θ_{qR} in terms of the experimentally measured scattering angles (θ_q, ϕ_q), and (θ, ϕ), the angle between the laser polarization and dipole transition axis and its corresponding azimuth:

$$P_n(\cos\theta_{qR}) = \frac{4\pi}{2n+1}\sum_{j=-k}^{k} Y^*_{jk}(\theta_q,\phi_q)Y_{jk}(\theta,\phi). \tag{A3}$$

We integrate over ϕ_q using scattering symmetry and use the above expressions to arrive at

$$\Delta\frac{d\sigma}{d\Omega} = 2(2\pi)^2\sigma_T \sum_{n=0,2,\ldots}(-1)^{n/2}P_n(\cos\theta_q)\Delta S_n(q), \tag{A4}$$

$$\begin{aligned}\Delta S_n(q,\tau) = \sum_{b\neq a} f_a^*(q) f_b(q)\int_{-1}^{1} d\cos(\theta)\\ \times \int_0^\infty dR R^2 \Delta\rho_{ab}(R,\cos(\theta),\tau)\\ \times P_n(\cos(\theta)) j_n(qR),\end{aligned} \tag{A5}$$

where $\Delta\rho_{ab}(R,\cos(\theta),\tau)$ is the time-dependent and angle-dependent pair density difference at time-delay τ. Scattering from a general anisotropic real-space charge will be manifested both by the intensity distribution on the detector via the scattering angle θ_q and via the anisotropy curves $\Delta S_n(q)$. To recover the anisotropic charge density of order n, we need to obtain $\Delta S_n(q)$ from the scattering pattern on the detector. This can be done by applying a Legendre decomposition over the detector angle θ_d described in Fig. 1. We decompose the 2D measured detector signal at delay time τ in each $[q,\theta_d]$ bin to an even-order Legendre basis up to the relevant significant order:

$$I(q,\theta_d,\tau) = \beta_0(q,\tau)\sum_{n=0,2,\ldots}\widetilde{\beta}_n(q,\tau)P_n(\cos\theta_d), \tag{A6}$$

where $\beta_0(q,\tau)$ is the radial detector intensity at delay τ, and $\widetilde{\beta}_n(q,\tau) = \beta_n(q,\tau)/\beta_0(q,\tau)$ are the normalized detector anisotropy terms. The relation between the nth-order anisotropy curve ΔS_n in Eq. (A5) and the corresponding $\beta_n(q,\tau)$ term was derived in a previous study [5], and is given by

$$\Delta S_n(q,\tau) = \frac{\beta_0(q,\tau)\widetilde{\beta}_n(q,\tau)}{\cos^n(\theta_q)} = \frac{\beta_n(q,\tau)}{\left(1-\frac{q^2}{4|k_0|^2}\right)^{n/2}}, \tag{A7}$$

where $|k_0|$ is the length of the wave vector of the incoming x-ray beam, $\beta_0(q,\tau)$ has units of intensity or the average number of scattered photons per q on the detector, whereas the anisotropic $\widetilde{\beta}_n(q,\tau)$ terms are dimensionless and represent ratios between intensities and different angles that govern the degree of anisotropy.

Direct real-space inversion and formation of NSKs will be applied to the measured ΔS_n in a similar way to that used for the isotropic case, where we need to generalize the expressions for distortions, discretization, and inversion to the anisotropic case.

1. NSK formalism for anisotropic scattering

The measurement constraints will create distortions on the retrieved anisotropic curves S_n that can be expressed as

$$\tilde{S}_n(q,\tau) = \int_{z_0-d}^{z_0+d} dz\, h_n(q(z))\, S_n(q(z),\tau) + b(q(z)), \tag{A8}$$

where $h_n(q)$ is a window function that contains angle dependence per anisotropy order n representing the detector's finite q-range as well as the q-dependent signal absorption. The discretization scheme for each anisotropy order n is given by

$$\left\{q_i^{(n)}\right\}_1^N = \frac{j_{ni}}{j_{nN}}N\Delta q, \quad \left\{R_m^{(n)}\right\}_1^M = \frac{j_{nm}}{M\Delta q}. \tag{A9}$$

We note that each anisotropy of order n is sampled at the corresponding spherical Bessel order j_n roots. As a result, different anisotropy orders will have slightly different sampling positions in q and R.

The distorted anisotropic difference scattering signal is discretized $\Delta\tilde{S}_n(q_i^{(n)},\tau)$, and the transformation back to real-space for the nth-order anisotropy is

$$\Delta \mathrm{PD}_n(R^{(n)},\tau) = \frac{[(M-1)\Delta q]^2}{j_{nM}}\sum_{i=1}^{M-1}\boldsymbol{G}^{(n)}_{mi}\frac{\Delta\tilde{S}_n\left(q_i^{(n)},\tau\right)q_i^{(n)}}{f_e\left(q_i^{(n)}\right)}, \tag{A10}$$

with the nth-order anisotropy transformation kernel:

$$[\boldsymbol{G}]^n_{mi} = 2\frac{j_n\left(\frac{j_{nm}j_{ni}}{j_{nM}}\right)}{j_{nM}\,j^2_{n+1}(j_{ni})}. \tag{A11}$$

The NSK for anisotropy order n for position $R_m^{(n)}$ is

$$\mathrm{NSK}_n\left(R_m^{(n)}\right) = \frac{[(M-1)\Delta q]^2}{j_{nM}}\sum_{i=1}^{M-1}\boldsymbol{G}^{(n)}_{mi}\,\tilde{j}_n\left(q_i^{(n)}R_m^{(n)}\right)q_i^{(n)}, \tag{A12}$$

where

$$\tilde{j}_n\left(q,R_m^{(n)}\right) = \int_{z_0-d}^{z_0+d} dz\, h_n(q(z))\, j_n\left(q(z)R_m^{(n)}\right). \tag{A13}$$

We can generate a group of dictionaries $\boldsymbol{\mathcal{D}}^{(n)}$, each containing a set of NSKs specific to a certain anisotropy order. These dictionaries will be used to approximate the charge density distributions for each anisotropy order. Inversion and deconvolution for each anisotropy order will then be performed using the previously mentioned regularization framework:

$$\min_{\mathrm{w}^{(n)}} \|\Delta\mathrm{PD}_n - \boldsymbol{\mathcal{D}}^{(n)}\mathbf{w}^{(n)}\|^2 + \epsilon\mathcal{R}(\mathbf{w}^{(n)}). \tag{A14}$$

To obtain the angle-resolved pair density from each anisotropic pair density solution $\mathbf{w}^{(n)}$, we need to resample $\mathbf{w}^{(n)}$ to the same real-space grid. We can then express the total pair density solution:

$$\mathbf{w}(R,\cos\theta) = \sum_{n=0,2,\ldots}\Delta P_n(\cos\theta)\tilde{\mathbf{w}}^{(n)}(R), \tag{A15}$$

where $\tilde{\mathbf{w}}^{(n)}(R)$ is the resampled $\mathbf{w}^{(n)}$ onto the isotropic real-space grid given by $R_m^{(0)}$.

2. Numerical example

Consider an ensemble of linear triatomic molecules that was photoexcited via absorbing a single photon, with a dipole transition parallel to the molecular axis creating a $\cos^2(\theta)$ angular distribution in the ensemble. This angular distribution is expressed by P_0 and P_2 Legendre polynomials in Eq. (A4). The scattering signal from the ensemble is the incoherent sum of scattering from single molecules, as we can neglect the

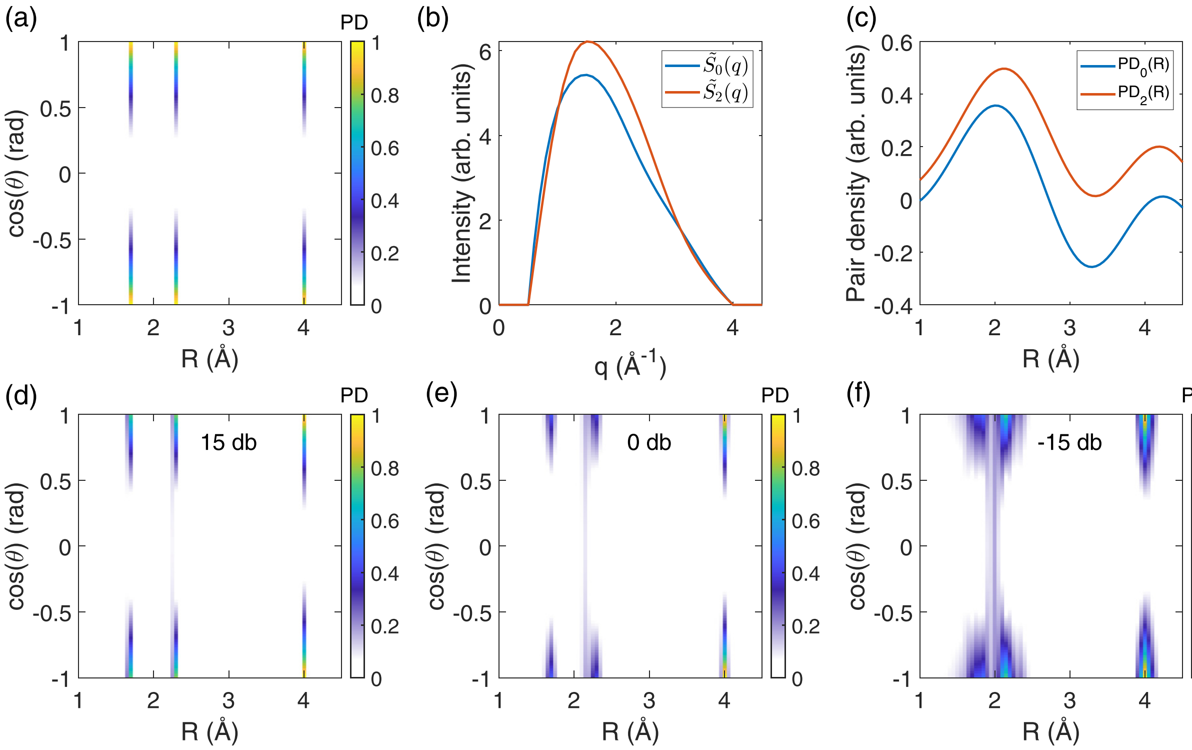

FIG. 6. Inversion and super-resolution of anisotropic charge density: (a) three pair-densities with $\cos^2(\theta)$ angular distribution at 1.7, 2.3, and 4 Å are obtained modeling an ensemble of triatomic molecules that was photoexcited (see the text). (b) The total simulated scattering is truncated and analyzed to obtain the scattering curves $\tilde{S}_n$. (c) The inversion of $\tilde{S}_n$ fails to retrieve the positions of the pair densities. We apply the NSK inversion and deconvolution using ℓ_1 regularization for each anisotropy order, and then we apply Eq. (A15) to obtain the angle- and space-resolved pair densities for SNR values of (d) 15, (e) 0, and (f) −15 dB. We super-resolve distances and angular distribution and observe that the pair coalescence effect takes place for the −15 dB case. At this SNR, the coalescence effect limits both the spatial and angle resolution for anisotropic scattering.

two-molecule scattering signal contribution because of their random positions. Thus, we can describe the charge density signal using the ensemble-averaged molecule picture. Borrowing from the example used for the isotropic case in Fig. 3, we set the atom positions versus the center of mass of each molecule to be at $x = -2$ Å for atom A, $x = 0.3$ Å for atom B, and $x = 2$ Å for atom C. The corresponding pair distances are $R_{AB} = 1.7$ Å, $R_{BC} = 2.3$ Å, and $R_{AC} = 4$ Å, each with a $\cos^2(\theta)$ angular distribution [Fig. 6(a)].

We simulated the scattering signal on a realistic detector, assuming detector pixel signal-to-noise (SNR) ratios of −15, 0, and 15 dB. We apply detector truncation restricting the range of measured signal to $0.5 < q < 4$ Å^{-1}. We note that using these parameters, the two pair distances R_{AB} and R_{BC} are 0.6 Å apart, below the diffraction limit of $\simeq$1.57 Å.

We retrieve the $\tilde{S}_n(q)$ curves using Eq. (A7) [Fig. 6(b)], and we invert to obtain PD$_n$ [Fig. 6(c)]. We form NSK$_n$ dictionaries for the zeroth- and second-order anisotropy, and we deconvolve PD$_n$ using Eq. (A14), with ℓ_1 regularization. The recoveries for each SNR are shown in Figs. 6(d)–6(f), capturing both positions and angular distributions of the pair densities. We obtain similar recovery accuracy and super-resolution conditions, limited by signal fidelity and pair coalescence. For the −15 db case, the coalescence effect for the angle-resolved pair density distances also obscures the angle information content related to their anisotropy, as seen as density broadening for $|\cos(\theta)| > 0.7$ and loss of anisotropy in the coalescence distance. This effect reflects the angular resolution limit in real-space recoveries of noisy signals.

---

[1] J. Küpper, S. Stern, L. Holmegaard, F. Filsinger, A. Rouzée, A. Rudenko, P. Johnsson, A. V. Martin, M. Adolph, A. Aquila *et al.*, X-Ray Diffraction from Isolated and Strongly Aligned Gas-Phase Molecules with a Free-Electron Laser, Phys. Rev. Lett. **112**, 083002 (2014).

[2] M. P. Minitti, J. M. Budarz, A. Kirrander, J. S. Robinson, D. Ratner, T. J. Lane, D. Zhu, J. M. Glownia, M. Kozina, H. T. Lemke, M. Sikorski, Y. Feng, S. Nelson, K. Saita, B. Stankus, T. Northey, J. B. Hastings, and P. M. Weber, Imaging Molecular Motion: Femtosecond X-Ray Scattering of an Electrocyclic Chemical Reaction, Phys. Rev. Lett. **114**, 255501 (2015).

[3] J. M. Glownia, A. Natan, J. P. Cryan, R. Hartsock, M. Kozina, M. P. Minitti, S. Nelson, J. Robinson, T. Sato, T. van Driel, G. Welch, C. Weninger, D. Zhu, and P. H. Bucksbaum, Self-Referenced Coherent Diffraction X-Ray Movie of

Ångstrom- and Femtosecond-Scale Atomic Motion, Phys. Rev. Lett. **117**, 153003 (2016).

[4] P. H. Bucksbaum, M. R. Ware, A. Natan, J. P. Cryan, and J. M. Glownia, Characterizing Multiphoton Excitation Using Time-Resolved X-ray Scattering, Phys. Rev. X **10**, 011065 (2020).

[5] A. Natan, A. Schori, G. Owolabi, J. P. Cryan, J. M. Glownia, and P. H. Bucksbaum, Resolving multiphoton processes with high-order anisotropy ultrafast x-ray scattering, Faraday Discuss. **228**, 123 (2021).

[6] T. Kierspel, A. Morgan, J. Wiese, T. Mullins, A. Aquila, A. Barty, R. Bean, R. Boll, S. Boutet, P. Bucksbaum *et al.*, X-ray diffractive imaging of controlled gas-phase molecules: Toward imaging of dynamics in the molecular frame, J. Chem. Phys. **152**, 084307 (2020).

[7] T. J. Wolf, D. M. Sanchez, J. Yang, R. Parrish, J. Nunes, M. Centurion, R. Coffee, J. Cryan, M. Gühr, K. Hegazy *et al.*, The photochemical ring-opening of 1, 3-cyclohexadiene imaged by ultrafast electron diffraction, Nat. Chem. **11**, 504 (2019).

[8] E. Champenois, D. Sanchez, J. Yang, J. Figueira Nunes, A. Attar, M. Centurion, R. Forbes, M. Gühr, K. Hegazy, F. Ji *et al.*, Conformer-specific photochemistry imaged in real space and time, Science **374**, 178 (2021).

[9] J. Yang, X. Zhu, J. P. F. Nunes, J. K. Yu, R. M. Parrish, T. J. Wolf, M. Centurion, M. Gühr, R. Li, Y. Liu *et al.*, Simultaneous observation of nuclear and electronic dynamics by ultrafast electron diffraction, Science **368**, 885 (2020).

[10] H. Ihee, M. Wulff, J. Kim, and S.-i. Adachi, Ultrafast x-ray scattering: structural dynamics from diatomic to protein molecules, Int. Rev. Phys. Chem. **29**, 453 (2010).

[11] K. H. Kim, J. G. Kim, S. Nozawa, T. Sato, K. Y. Oang, T. W. Kim, H. Ki, J. Jo, S. Park, C. Song *et al.*, Direct observation of bond formation in solution with femtosecond x-ray scattering, Nature (London) **518**, 385 (2015).

[12] E. Biasin, T. B. van Driel, K. S. Kjær, A. O. Dohn, M. Christensen, T. Harlang, P. Vester, P. Chabera, Y. Liu, J. Uhlig, M. Pápai, Z. Németh, R. Hartsock, W. Liang, J. Zhang, R. Alonso-Mori, M. Chollet, J. M. Glownia, S. Nelson, D. Sokaras *et al.*, Femtosecond x-ray Scattering Study of Ultrafast Photoinduced Structural Dynamics in Solvated $[\mathrm{Co(terpy)}_2]^{2+}$, Phys. Rev. Lett. **117**, 013002 (2016).

[13] T. B. Van Driel, K. S. Kjær, R. W. Hartsock, A. O. Dohn, T. Harlang, M. Chollet, M. Christensen, W. Gawelda, N. E. Henriksen, J. G. Kim *et al.*, Atomistic characterization of the active-site solvation dynamics of a model photocatalyst, Nat. Commun. **7**, 13678 (2016).

[14] M. Chollet, R. Alonso-Mori, M. Cammarata, D. Damiani, J. Defever, J. T. Delor, Y. Feng, J. M. Glownia, J. B. Langton, S. Nelson *et al.*, The x-ray pump-probe instrument at the linac coherent light source, J. Synchrotron Radiat. **22**, 503 (2015).

[15] K. Haldrup, G. Levi, E. Biasin, P. Vester, M. G. Laursen, F. Beyer, K. S. Kjær, T. Brandt van Driel, T. Harlang, A. O. Dohn, R. J. Hartsock, S. Nelson, J. M. Glownia, H. T. Lemke, M. Christensen, K. J. Gaffney, N. E. Henriksen, K. B. Møller, and M. M. Nielsen, Ultrafast X-Ray Scattering Measurements of Coherent Structural Dynamics on the Ground-State Potential Energy Surface of a Diplatinum Molecule, Phys. Rev. Lett. **122**, 063001 (2019).

[16] M. R. Panman, E. Biasin, O. Berntsson, M. Hermann, S. Niebling, A. J. Hughes, J. Kübel, K. Atkovska, E. Gustavsson, A. Nimmrich, A. O. Dohn, M. Laursen, D. B. Zederkof, A. Honarfar, K. Tono, T. Katayama, S. Owada, T. B. van Driel, K. Kjaer, M. M. Nielsen *et al.*, Observing the Structural Evolution in the Photodissociation of Diiodomethane with Femtosecond Solution X-Ray Scattering, Phys. Rev. Lett. **125**, 226001 (2020).

[17] B. Stankus, H. Yong, N. Zotev, J. M. Ruddock, D. Bellshaw, T. J. Lane, M. Liang, S. Boutet, S. Carbajo, J. S. Robinson *et al.*, Ultrafast x-ray scattering reveals vibrational coherence following rydberg excitation, Nat. Chem. **11**, 716 (2019).

[18] S. W. Hell and J. Wichmann, Breaking the diffraction resolution limit by stimulated emission: stimulated-emission-depletion fluorescence microscopy, Opt. Lett. **19**, 780 (1994).

[19] E. Betzig, G. H. Patterson, R. Sougrat, O. W. Lindwasser, S. Olenych, J. S. Bonifacino, M. W. Davidson, J. Lippincott-Schwartz, and H. F. Hess, Imaging intracellular fluorescent proteins at nanometer resolution, Science **313**, 1642 (2006).

[20] Y. M. Sigal, R. Zhou, and X. Zhuang, Visualizing and discovering cellular structures with super-resolution microscopy, Science **361**, 880 (2018).

[21] M. A. Phillips, M. Harkiolaki, D. M. S. Pinto, R. M. Parton, A. Palanca, M. Garcia-Moreno, I. Kounatidis, J. W. Sedat, D. I. Stuart, A. Castello *et al.*, Cryosim: super-resolution 3d structured illumination cryogenic fluorescence microscopy for correlated ultrastructural imaging, Optica **7**, 802 (2020).

[22] A. Sroda, A. Makowski, R. Tenne, U. Rossman, G. Lubin, D. Oron, and R. Lapkiewicz, Sofism: Super-resolution optical fluctuation image scanning microscopy, Optica **7**, 1308 (2020).

[23] U. Lorenz, K. B. Møller, and N. E. Henriksen, Theory of time-resolved inelastic x-ray diffraction, Phys. Rev. A **81**, 023422 (2010).

[24] M. Simmermacher, N. E. Henriksen, K. B. Møller, A. Moreno Carrascosa, and A. Kirrander, Electronic Coherence in Ultrafast X-Ray Scattering from Molecular Wave Packets, Phys. Rev. Lett. **122**, 073003 (2019).

[25] U. Lorenz, K. B. Møller, and N. E. Henriksen, On the interpretation of time-resolved anisotropic diffraction patterns, New J. Phys. **12**, 113022 (2010).

[26] P. Debye, Zerstreuung von röntgenstrahlen, Ann. Phys. **351**, 809 (1915).

[27] A. O. Dohn, E. Biasin, K. Haldrup, M. M. Nielsen, N. E. Henriksen, and K. B. Møller, On the calculation of x-ray scattering signals from pairwise radial distribution functions, J. Phys. B **48**, 244010 (2015).

[28] F. t. Zernike and J. Prins, Die beugung von röntgenstrahlen in flüssigkeiten als effekt der molekülanordnung, Z. Phys. Phys. A **41**, 184 (1927).

[29] J. C. Williamson and A. H. Zewail, Ultrafast electron diffraction. 4. molecular structures and coherent dynamics, J. Phys. Chem. **98**, 2766 (1994).

[30] J. Budarz, M. Minitti, D. Cofer-Shabica, B. Stankus, A. Kirrander, J. Hastings, and P. Weber, Observation of femtosecond molecular dynamics via pump–probe gas phase x-ray scattering, J. Phys. B **49**, 034001 (2016).

[31] T. B. Van Driel, S. Nelson, R. Armenta, G. Blaj, S. Boo, S. Boutet, D. Doering, A. Dragone, P. Hart, G. Haller *et al.*, The epix10k 2-megapixel hard x-ray detector at lcls, J. Synchrotron Radiat. **27**, 608 (2020).

[32] E. Lorch, Neutron diffraction by germania, silica and radiation-damaged silica glasses, J. Phys. C **2**, 229 (1969).

[33] N. Baddour and U. Chouinard, Theory and operational rules for the discrete hankel transform, J. Opt. Soc. Am. A **32**, 611 (2015).

[34] C. E. Shannon, Communication in the presence of noise, Proc. IRE **37**, 10 (1949).

[35] E. J. Candès, J. Romberg, and T. Tao, Robust uncertainty principles: Exact signal reconstruction from highly incomplete frequency information, IEEE Trans. Inf. Theor. **52**, 489 (2006).

[36] P. C. Hansen and D. P. OLeary, The use of the l-curve in the regularization of discrete ill-posed problems, SIAM J. Sci. Comput. **14**, 1487 (1993).

[37] S. Arlot and A. Celisse, A survey of cross-validation procedures for model selection, Statist. Surv. **4**, 40 (2010).

[38] G. H. Golub, P. C. Hansen, and D. P. O'Leary, Tikhonov regularization and total least squares, SIAM J. Matrix Anal. Appl. **21**, 185 (1999).

[39] S. Chen and D. Donoho, Basis pursuit, in *Proceedings of 1994 28th Asilomar Conference on Signals, Systems and Computers* (IEEE, Piscataway, NJ, 1994), Vol. 1, pp. 41–44.

[40] R. Tibshirani, Regression shrinkage and selection via the lasso, J. R. Statist. Soc.: Ser. B (Methodological) **58**, 267 (1996).

[41] S. Boyd, N. Parikh, and E. Chu, *Distributed Optimization and Statistical Learning via the Alternating Direction Method of Multipliers* (Now Publishers, 2011).

[42] N. Parikh and S. Boyd, Proximal algorithms, Found. Trends Optimization **1**, 127 (2014).

[43] E. J. Candès and J. Romberg, l1-Magic Recovery of Sparse Signals via Convex Programming (unpublished).

[44] H. Lee, A. Battle, R. Raina, and A. Y. Ng, Efficient sparse coding algorithms, in *Advances in Neural Information Processing Systems* (Citeseer MIT Press, Cambridge, MA, USA, 2007), pp. 801–808.

[45] J. Mairal, F. Bach, J. Ponce, and G. Sapiro, Online dictionary learning for sparse coding, in *Proceedings of the 26th Annual International Conference on Machine Learning* (Association for Computing Machinery, New York, NY, USA, 2009), pp. 689–696.

[46] K. Gregor and Y. LeCun, Learning fast approximations of sparse coding, in *Proceedings of the 27th International Conference on Machine Learning* (Omnipress, Madison, WI, USA, 2010), pp. 399–406.

[47] D. L. Donoho, Compressed sensing, IEEE Trans. Inf. Theor. **52**, 1289 (2006).

[48] M. Lustig, D. Donoho, and J. M. Pauly, Sparse mri: The application of compressed sensing for rapid mr imaging, Magn. Res. Med.: **58**, 1182 (2007).

[49] M. F. Duarte, M. A. Davenport, D. Takhar, J. N. Laska, T. Sun, K. F. Kelly, and R. G. Baraniuk, Single-pixel imaging via compressive sampling, IEEE Sign. Proc. Mag. **25**, 83 (2008).

[50] O. Katz, Y. Bromberg, and Y. Silberberg, Compressive ghost imaging, Appl. Phys. Lett. **95**, 131110 (2009).

[51] Y. Shechtman, S. Gazit, A. Szameit, Y. C. Eldar, and M. Segev, Super-resolution and reconstruction of sparse images carried by incoherent light, Opt. Lett. **35**, 1148 (2010).

[52] O. Solomon, M. Mutzafi, M. Segev, and Y. C. Eldar, Sparsity-based super-resolution microscopy from correlation information, Opt. Express **26**, 18238 (2018).

[53] A.-X. Zhang, Y.-H. He, L.-A. Wu, L.-M. Chen, and B.-B. Wang, Tabletop x-ray ghost imaging with ultra-low radiation, Optica **5**, 374 (2018).

[54] T. Driver, S. Li, E. G. Champenois, J. Duris, D. Ratner, T. J. Lane, P. Rosenberger, A. Al-Haddad, V. Averbukh, T. Barnard *et al.*, Attosecond transient absorption spooktroscopy: a ghost imaging approach to ultrafast absorption spectroscopy, Phys. Chem. Chem. Phys. **22**, 2704 (2020).

[55] M. Grant and S. Boyd, Cvx: Matlab software for disciplined convex programming, version 2.1 (2014).

[56] E. J. Candès and C. Fernandez-Granda, Super-resolution from noisy data, J. Fourier Anal. Appl. **19**, 1229 (2013).

[57] C. Fernandez-Granda, Super-resolution of point sources via convex programming, Information and Inference: J. IMA **5**, 251 (2016).

[58] V. Duval and G. Peyré, Exact support recovery for sparse spikes deconvolution, Found. Computat. Math. **15**, 1315 (2015).

[59] H. Zou and T. Hastie, Regularization and variable selection via the elastic net, J. R. Stat. Soc.: Ser. B **67**, 301 (2005).

[60] P. Catala, V. Duval, and G. Peyré, A low-rank approach to off-the-grid sparse superresolution, SIAM J. Imag. Sci. **12**, 1464 (2019).

[61] G. Dixit, O. Vendrell, and R. Santra, Imaging electronic quantum motion with light, Proc. Natl. Acad. Sci. (USA) **109**, 11636 (2012).

[62] D. Popova-Gorelova and R. Santra, Imaging interatomic electron current in crystals with ultrafast resonant x-ray scattering, Phys. Rev. B **92**, 184304 (2015).

[63] M. Kowalewski, K. Bennett, and S. Mukamel, Monitoring nonadiabatic avoided crossing dynamics in molecules by ultrafast x-ray diffraction, Struct. Dyn. **4**, 054101 (2017).

[64] D. Popova-Gorelova, D. A. Reis, and R. Santra, Theory of x-ray scattering from laser-driven electronic systems, Phys. Rev. B **98**, 224302 (2018).

[65] M. Simmermacher, A. Moreno Carrascosa, N. E. Henriksen, K. B. Møller, and A. Kirrander, Theory of ultrafast x-ray scattering by molecules in the gas phase, J. Chem. Phys. **151**, 174302 (2019).

[66] G. Hermann, V. Pohl, G. Dixit, and J. C. Tremblay, Probing Electronic Fluxes via Time-Resolved X-Ray Scattering, Phys. Rev. Lett. **124**, 013002 (2020).

[67] A. Sánchez, K. Amini, S.-J. Wang, T. Steinle, B. Belsa, J. Danek, A.-T. Le, X. Liu, R. Moshammer, T. Pfeifer *et al.*, Molecular structure retrieval directly from laboratory-frame photoelectron spectra in laser-induced electron diffraction, Nat. Commun. **12**, 1 (2021).

[68] E. Biasin, T. B. Van Driel, G. Levi, M. G. Laursen, A. O. Dohn, A. Moltke, P. Vester, F. B. Hansen, K. S. Kjaer, T. Harlang *et al.*, Anisotropy enhanced x-ray scattering from solvated transition metal complexes, J. Synch. Radiat. **25**, 306 (2018).

[69] J. Yang, X. Zhu, T. J. Wolf, Z. Li, J. P. F. Nunes, R. Coffee, J. P. Cryan, M. Gühr, K. Hegazy, T. F. Heinz *et al.*, Imaging cf3i conical intersection and photodissociation dynamics with ultrafast electron diffraction, Science **361**, 64 (2018).